

# Nanomechanical pump-probe measurements of insulating electronic states in a carbon nanotube

Ilya Khivrich<sup>1</sup>, Aashish A. Clerk<sup>2</sup> and Shahal Ilani <sup>1\*</sup>

**Transport measurements have been an indispensable tool in studying conducting states of matter. However, there exists a large set of interesting states that are insulating, often due to electronic interactions or topology, and are difficult to probe via transport. Here, through an experiment on carbon nanotubes, we present a new approach capable of measuring insulating electronic states through their back action on nanomechanical motion. We use a mechanical pump-probe scheme, allowing the detection of shifts in both frequency and dissipation rate of mechanical vibrational modes, in an overall insulating system. As an example, we use this method to probe the non-conducting configurations of a double quantum dot, allowing us to observe the theoretically predicted signature of nanomechanical back action resulting from a coherently tunnelling electron. The technique opens a new way for measuring the internal electronic structure of a growing variety of insulating states in one- and two-dimensional systems.**

In recent years, a growing number of strongly correlated insulating electronic states have been discovered in low-dimensional systems. In carbon-based systems alone, for example, there are the Mott insulator<sup>1</sup>, the Wigner crystal<sup>2–4</sup> and the proposed excitonic insulator<sup>5</sup> in one dimension (carbon nanotubes), as well as symmetry-broken states<sup>6</sup> and the magic-angle Mott insulating state<sup>7</sup> in two dimensions (bilayer graphene). However, since these states are non-conducting, to study them one needs a tool that goes beyond transport, and is able to probe their internal charge and spin degrees of freedom on local scales. So far, capacitive-based techniques such as coupling to microwave cavities<sup>8</sup> or to single-electron transistor charge detectors<sup>9</sup> have proved instrumental in studying local electron dynamics in simple non-conducting systems on the single-electron level.

Coupling to nanomechanics<sup>10</sup> can provide an especially sensitive way for probing these insulating states. Indeed, many systems that exhibit non-trivial insulating behaviour can be made suspended, allowing their own mechanical motion to probe their local electronic degrees of freedom. Similar to coupling to a microwave cavity, coupling to a mechanical cavity can probe the electronic degrees of freedom, with a few key features: mechanics couples to force rather than charge, and can thus probe both charge and spin degrees of freedom<sup>11</sup>. Nanomechanical resonators can have large quality factors<sup>12,13</sup>, resulting in extreme force sensitivity<sup>14</sup>. Since mechanical modes are determined by the speed of sound rather than the speed of light as in microwave cavities, they are more localized in space, yielding stronger couplings in smaller dimensions. Nanomechanical experiments have indeed been extremely successful in measuring the interactions with single electrons in quantum dots<sup>12,13,15–27</sup> and with two-dimensional electronic systems<sup>6</sup>. However, to date, all these experiments have relied on electronic transport for their operation, and thus could not probe insulating electronic states, limiting their scope.

In this work, we introduce a new time-domain technique for measuring insulating electronic states via coupling to nanomechanical motion. The technique, demonstrated on a carbon nanotube (NT), allows the measurement of frequency shifts and dissipation

rates of the mechanical vibrations due to back action of the electronic degrees of freedom in the system, even when the system is not conducting overall. As an example, we use this technique to probe a double quantum dot in the regime where no current can flow through the device, and demonstrate the recently predicted<sup>28</sup> signature of mechanical coupling to an electron that coherently tunnels between the dots, going beyond existing experiments that could observe the back action due only to incoherent tunneling.

The device in this study consists of a single carbon NT, assembled<sup>29</sup> on source and drain contact electrodes and suspended above seven gates (suspension length  $L=1.2\ \mu\text{m}$ ), being free to vibrate (Fig. 1a). Individual DC voltages are applied on the seven gates, controlling the electrostatic potential landscape along the NT. An arbitrary wave generator is connected to the source electrode and the three central gates via wide-band bias-Ts (not shown), generating radiofrequency pulses for actuating and measuring the NT mechanical motion, as well as for applying fast gate voltage traverses. To measure the current through the NT, we use two methods. The first is a standard quasi-DC measurement, where the current at the drain is measured with a low-bandwidth current preamplifier. The second, adopted from shot noise experiments<sup>30</sup>, uses an LC tank circuit coupled to a high electron mobility transistor (HEMT) amplifier at the cryogenic stage, which allows one to shift the readout to a higher frequency ( $f_{\text{tank}} = 1.45\ \text{MHz}$ ) and increase the bandwidth (30 kHz full-width at half-maximum). At the room-temperature stage, the signal is amplified, down-converted using an IQ demodulator, simultaneously with a phase reference signal, then sampled and processed using custom software (details in Supplementary Section 2).

We study both single and double quantum dot configurations, formed on the suspended part of the NT. Since the assembled NT has negligible electronic disorder (Supplementary Section 1), these configurations can be readily formed by tuning the gate voltages. In a single quantum dot configuration (Fig. 1b, top), the central part of the NT is gated to be p-doped (red), while the workfunction difference ( $\sim 250\ \text{meV}$ ) between the NT and Au contacts creates n-doped regions of the NT above the contacts (blue). Due to the

<sup>1</sup>Department of Condensed Matter Physics, Weizmann Institute of Science, Rehovot, Israel. <sup>2</sup>Institute for Molecular Engineering, University of Chicago, Chicago, IL, USA. \*e-mail: [shahal.ilani@weizmann.ac.il](mailto:shahal.ilani@weizmann.ac.il)

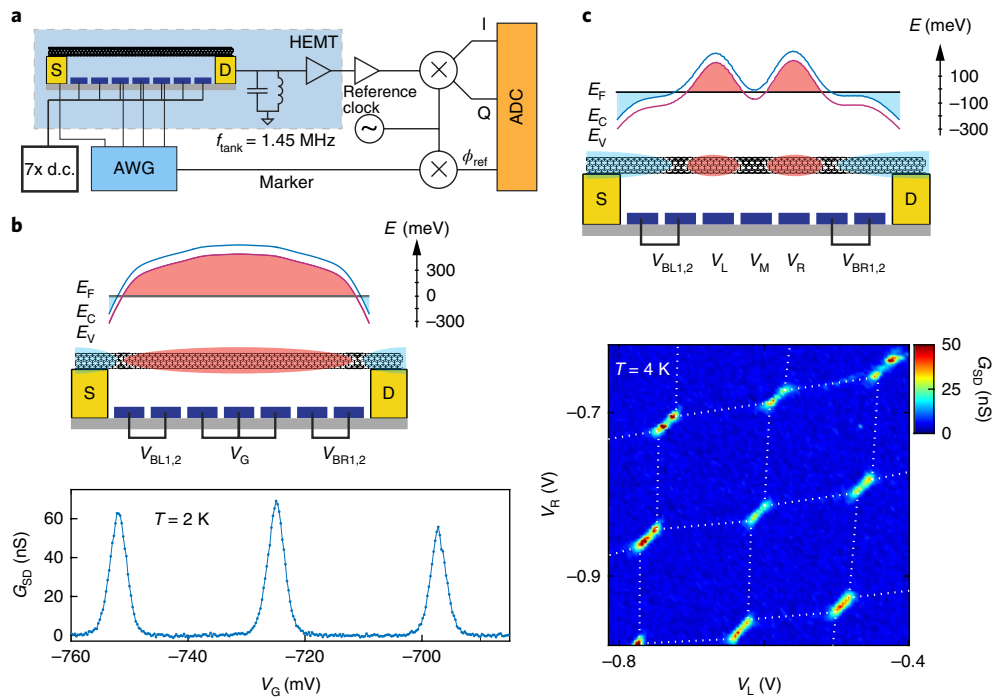


**Fig. 1 | Measurement set-up and transport characterization of carbon NT devices.** **a**, Illustration of the measurement set-up: the device consists of a single carbon NT, suspended over a length  $L = 1.2 \mu\text{m}$  between two contacts (source S, drain D) and over seven gates. Independent d.c. voltage sources are applied to the gates. Four channels of an arbitrary wave generator (AWG) are connected to the three central gates and the source. We alternate between two methods for measuring the current through the NT: a standard quasi-d.c. measurement with a current preamplifier connected at the drain (not shown), or a measurement at a higher carrier frequency using a cryogenic tank circuit connected at the drain, after which the signal is amplified by a cryogenic HEMT and a room-temperature amplifier. The resulting signal is demodulated and sampled simultaneously with a phase synchronization signal ( $\phi_{\text{ref}}$ ). ADC, analogue to digital converter; I, in-phase; Q, quadrature. **b**, Simulated band bending diagram of a single quantum dot configuration in our experiment, created by tuning the gate voltages to obtain a p-doped island (red) separated by pn junctions from n-doped leads (blue). Voltage  $V_G$ , applied on the three central gates, controls the occupation of the dot, while  $V_{\text{BL},2}$ ,  $V_{\text{BR},2}$  can be used to tune the barriers. Bottom: measured device conductance,  $G_{\text{SD}}$ , as a function of  $V_G$ . **c**, Simulated band bending diagram of the double quantum dot configuration in our experiment. Here a third barrier is formed by tuning  $V_M$  so that the NT segment above it is in the gap. Voltages  $V_L$  and  $V_R$  control the occupation of the two dots. Bottom: device conductance measured as a function of  $V_L$  and  $V_R$ .

small but sizeable bandgap of the NT ( $\sim 60 \text{ meV}$ ), pn junctions are formed between the central island and the leads, acting as tunnelling barriers. A common voltage  $V_G$  on three central gates controls the occupation of the resulting quantum dot. The tunnelling barriers between the dot and the leads are tuned using the two pairs of rightmost and leftmost gates  $V_{\text{BL}}$ ,  $V_{\text{BR}}$  (Fig. 1b, top). The measured conductance,  $G_{\text{SD}}$ , at  $T = 2 \text{ K}$ , shows regular Coulomb blockade oscillations (Fig. 1b, bottom). To form a double dot, we create an additional central barrier by tuning  $V_M$  so that the section of the NT above the central gate is in the gap (Fig. 1c, top). Gate voltages  $V_R$  and  $V_L$  control the occupation of the two dots. Measurement of  $G_{\text{SD}}$ , as a function of  $V_L$  and  $V_R$  at  $T = 4.2 \text{ K}$  (Fig. 1c, bottom), shows the standard double-dot charge stability diagram<sup>31</sup>, where conductance appears only at triple points in which the electronic transitions across the right, centre and left barriers (dashed white lines) are energetically available simultaneously. In all other regions of the charge stability diagram, a double quantum dot is not conducting (that is,  $G_{\text{SD}} = 0$ ). In these regions, it is thus impossible to detect any behaviour of the electronic system using transport or steady-state nanomechanical measurements.

### Continuous-wave and pump-probe measurement

To explain our measurement scheme, we start with the simpler case of a single quantum dot coupled to the mechanical motion of the NT (lowest mechanical mode). This system has been studied extensively in the past, mostly via the ‘mixing technique’<sup>32</sup>,

which uses the transport through the NT under continuous-wave (CW) excitations to probe its mechanical motion. Figure 2a shows such a measurement for our device. We apply CW voltage tones on the gate ( $V_{\text{pump}}^{\text{CW}} = A_{\text{pump}} \cos(\omega_{\text{pump}} t)$ ) and on the source ( $V_{\text{probe}}^{\text{CW}} = A_{\text{probe}} \cos(\omega_{\text{probe}} t)$ ). When the pump frequency hits a mechanical resonance of the NT, it drives it into mechanical oscillations, which modulate the capacitance of the quantum dot to the gate, acting effectively as an oscillating gate voltage. The sharp dependence of the dot’s conductance on the gate voltage near a Coulomb blockade peak leads to a mixed-tone signal,  $I_{\text{out}}$ , measured at the beat tone,  $\omega_{\text{pump}} - \omega_{\text{probe}}$  (colour map, Fig. 2a). Tracking the gate dependence of the first mechanical mode frequency, we find electromechanical softening around Coulomb blockade peaks, as observed previously<sup>24,25</sup>. From the frequency dependence of the two quadratures of  $I_{\text{out}}$  (Fig. 2b), taken along the dashed line in Fig. 2a, we extract the first mechanical mode frequency,  $\omega_1 = 2\pi \times 185.18 \text{ MHz}$ , and its quality factor  $Q = 1.1 \times 10^4$ . The dependence of  $Q^{-1}$  on the actuating amplitude (Fig. 2c) establishes that, at the measurement amplitude used throughout this figure ( $A_{\text{pump}} = 0.3 \text{ mV}$ , red dashed line), the motion is in the linear regime (Supplementary Section 4).

We now introduce a pump-probe variant of the above technique. Instead of using continuous waves, we split the pump (gate) and probe (source) signals in time. The measurement consists of four consecutive steps (Fig. 2d). First, the mechanical motion is actuated

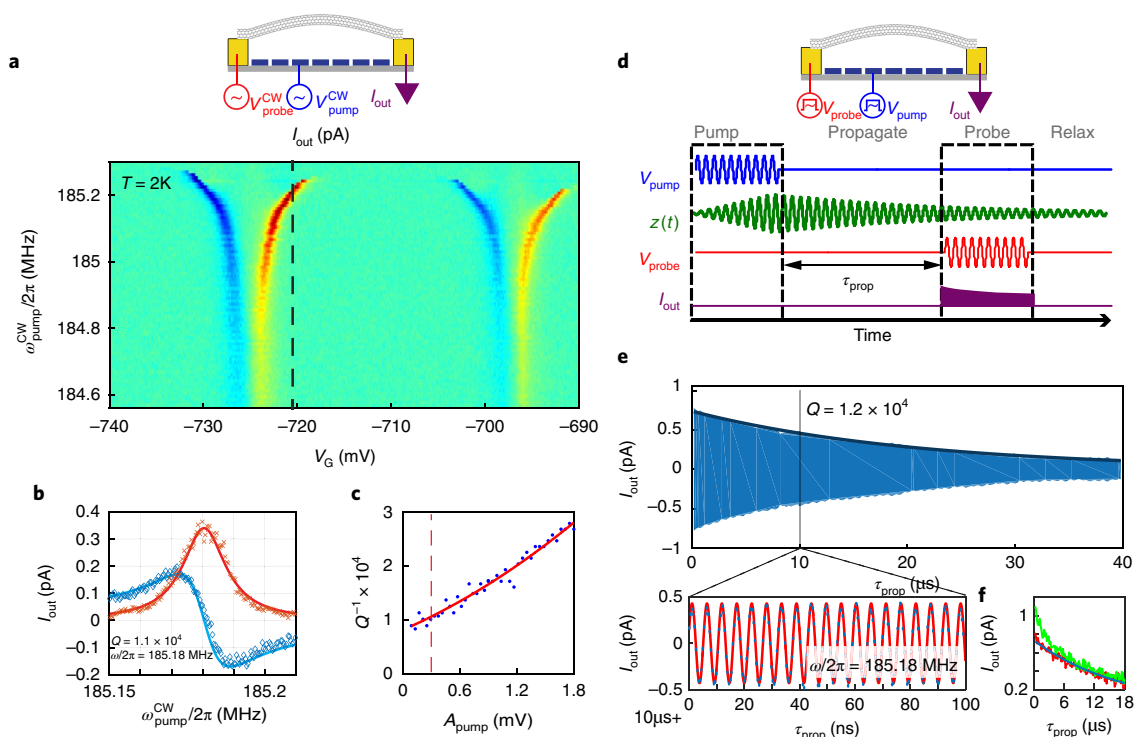


**Fig. 2 | Nanomechanical measurements of conducting states in a single quantum dot configuration.** **a**, Standard ‘mixing technique’ measurement scheme<sup>32</sup>: CW radiofrequency signals are applied on the gate and the source,  $V_{\text{pump}}^{\text{CW}} = A_{\text{pump}} \cos(\omega_{\text{pump}} t)$  and  $V_{\text{probe}}^{\text{CW}} = A_{\text{probe}} \cos(\omega_{\text{probe}} t)$ , and the current at their beat frequency,  $I_{\text{out}} \sim \cos((\omega_{\text{pump}} - \omega_{\text{probe}})t)$ , is measured at the drain. (Bottom) Measured out-of-phase quadrature of  $I_{\text{out}}$  as a function of  $V_G$  and  $\omega_{\text{pump}}^{\text{CW}}$ . Ridges of enhanced signal trace the gate voltage dependence of the first mechanical mode of the NT,  $T = 2\text{ K}$ . **b**, In-phase (blue) and out-of-phase (red) quadratures of  $I_{\text{out}}$ , measured as a function of  $\omega_{\text{pump}}^{\text{CW}}$  along the dashed line in **a**. From Lorentzian fits (solid line), the frequency of the mechanical mode,  $\omega/2\pi = 185.18\text{ MHz}$  and its quality factor,  $Q = 1.1 \times 10^4$ , are extracted. **c**, Inverse quality factor,  $Q^{-1}$ , measured as a function of  $A_{\text{pump}}$ . Solid line is a parabolic fit. The measurements in **a** are done at  $A_{\text{pump}} = 0.3\text{ mV}$  (red dashed line), to remain in the linear response regime. **d**, Pump-probe measurements of the nanomechanical response of a conducting state (same  $V_G$  as in **b**). The measurement sequence has four steps. First, an AC voltage pulse resonant with the mechanical mode frequency is applied on one of the gates ( $V_{\text{pump}}$  blue), causing the instantaneous amplitude of the NT motion ( $z(t)$ , green) to ramp up. Then, the resonator is allowed to propagate freely for  $\tau_{\text{prop}}$ . Next, an a.c. probe tone (red) is applied on the source, mixing down with the gating due to the residual mechanical motion, to produce a current pulse,  $I_{\text{out}}$  (purple) measured at the drain. Finally, the system is left to relax for time  $\tau_{\text{relax}}$ . **e**,  $I_{\text{out}}$  measured as a function of  $\tau_{\text{prop}}$ , showing exponential decay with  $Q = 1.2 \times 10^4$  of the mechanical motion amplitude (black fit line). (Inset) Zoom-in to short timescales, revealing rapid oscillations of  $I_{\text{out}}$  (blue dots) due to the phase difference between the mechanical motion and the probe pulse, with a frequency  $\omega/2\pi = 185.18\text{ MHz}$  (red line), identical to that measured by CW methods in **b**. **f**, Amplitude decay as a function of  $\tau_{\text{prop}}$  for  $A_{\text{pump}}$  above (green) and below (red) the nonlinearity threshold. Exponential decay (blue) is obtained in the linear regime.

with a radiofrequency pulse on the gate, resonant with one of the NT’s mechanical resonances (pump step). Next, the NT is allowed to oscillate freely for a time  $\tau_{\text{prop}}$  (free propagation step). During this step the oscillation decays with characteristic time  $Q/\omega_n$  (where  $Q$  is the quality factor of the mechanical resonance). Then, we interrogate the amplitude and phase of the residual mechanical motion using a probe pulse at a frequency close to the resonance frequency (shifted by  $f_{\text{tank}}$  if radiofrequency readout is used), applied on the source electrode (probe step). Similar to the CW mixing technique, the residual mechanical motion will act as an oscillating gate voltage at the mechanical mode frequency, and will mix down with the probe pulse to produce a current pulse at the drain,  $I_{\text{out}}$ , whose amplitude is proportional to the amplitude of the mechanical motion. Crucially, since both the probe and pump pulses start from zero phase, the phase difference between the probe pulse and the mechanical motion is deterministic for each repetition of the experiment, and thus the measured  $I_{\text{out}}$  will oscillate as a function of  $\tau_{\text{prop}}$ , tracking the phase of the mechanical motion. In the last segment (relaxation step) the NT mechanical motion is left to relax for a time  $\tau_{\text{relax}}$ , and the sequence is repeated in a periodic manner. In the actual experiments, we use lock-in variants of this protocol,

detailed in Supplementary Section 2, substantially improving the detection sensitivity.

Figure 2e shows the measured  $I_{\text{out}}$  as a function of  $\tau_{\text{prop}}$  for a NT with a single quantum dot driven at its first mechanical resonance frequency, revealing its mechanical ringdown. This measurement is done at the same  $V_G$  as in the CW measurements in Fig. 2b. The timing parameters are chosen so that  $\tau_{\text{pump}} = 4\text{ }\mu\text{s}$ ,  $\tau_{\text{probe}} = 8\text{ }\mu\text{s}$  are both comparable to  $Q/\omega_1$ . The full measurement cycle is chosen to be on a longer timescale to reduce interference between repetitions:  $\tau_{\text{pump}} + \tau_{\text{probe}} + \tau_{\text{prop}} + \tau_{\text{relax}} = 56\text{ }\mu\text{s}$ . The pump amplitude is chosen as to avoid nonlinear driving (see Supplementary Section 2) and the probe amplitude is chosen to be smaller than the width of the Coulomb blockade peak. The measured signal exhibits an exponentially decaying envelope that reflects the dissipation of the mechanical motion. The quality factor of this ringdown,  $Q = 1.2 \times 10^4$ , matches nicely the one measured by CW methods. Zooming in to a short time interval (Fig. 2e, inset) reveals fast oscillations at the frequency of the mechanical mode. Figure 2f shows the measured ringdown as a function of  $A_{\text{pump}}$ , demonstrating that at weak driving (red) the decay follows a simple exponential, and deviates from that only at strong driving (green), allowing

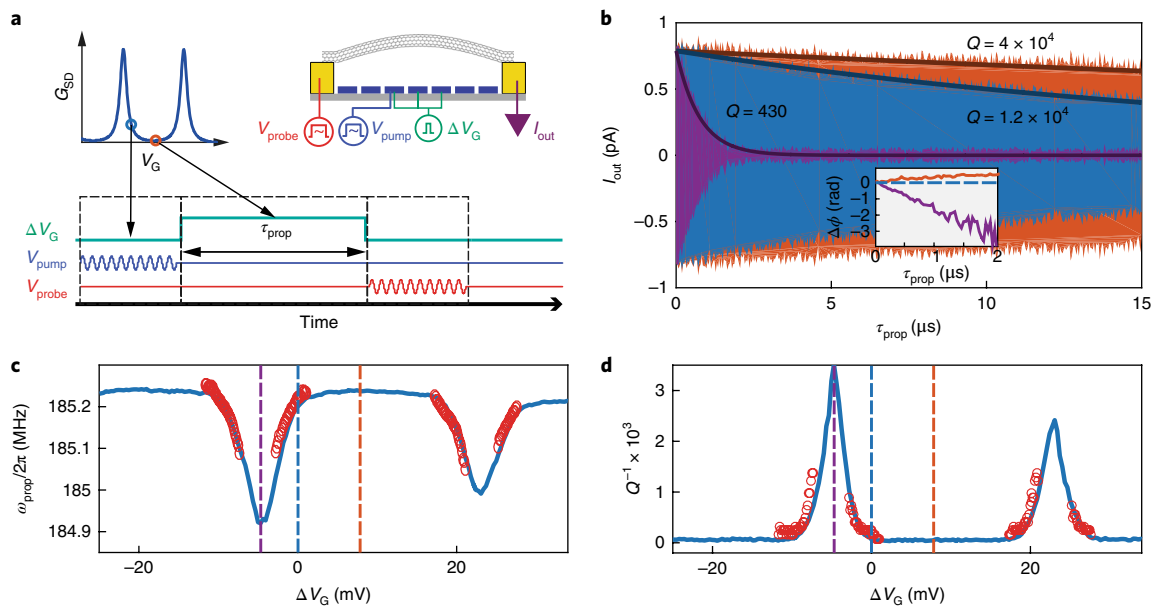


**Fig. 3 | Nanomechanical measurements of insulating states in a single quantum dot configuration.** **a**, Schematic time sequence: in addition to the radiofrequency pulses in Fig. 2d, we now also apply fast voltage steps,  $\Delta V_G$ , on the gate. The latter makes a fast traverse between a conducting point at the flank of the Coulomb peak (blue circle, top sketch) used in the pump, probe, and relax stages, and any generic gate voltage point during the free propagation stage, including ones in an insulating state (for example, the red circle in the top sketch). **b**, Ringdowns measured for  $\Delta V_G = 0$  mV,  $-4.4$  mV,  $7.8$  mV with respect to the pumping point (blue, purple, orange). Exponential decay fits (black lines) give the corresponding quality factors. Inset: the phase of  $I_{out}$ ,  $\Delta\phi$ , measured as a function of  $\tau_{prop}$  for these three ringdowns. **c,d**, Extracted gate voltage dependence of the first mode resonance frequency (**c**) and quality factor (**d**). Red circles are obtained from the CW mixing technique (data from Fig. 2a) and the blue trace is obtained using the time-domain technique described above. The two techniques match where both can measure, whereas only the time-domain technique can measure when  $G_{SD}$  is zero (Coulomb valley) or is gate independent (tip of Coulomb blockade peak).

us to determine the linear driving regime and limit our measurements to it.

### Time-domain scheme for probing insulating states

Similar to the conventional mixing technique, the time-domain variant described above has a major limitation—it relies on transport through the NT for detecting its motion, and thus it cannot work when the NT is electronically insulating. We alleviate this limitation by realizing that the above scheme actually measures the electromechanical interactions that occur during the free propagation stage, and during this stage the system can be in an insulating state. Transport is needed only for reading out the oscillator state at the final (probe) step. Thus, if we can rapidly gate the system between an insulating state for the experiment and a conducting state for the readout, we should be able to measure the mechanical back action within the insulating state. The corresponding measurement protocol is shown in Fig. 3a: the mechanical motion is first pumped at a conducting point on the Coulomb blockade. Then, the voltage  $V_G$  is rapidly ramped into an insulating point in the Coulomb valley, followed by the free propagation stage. Finally,  $V_G$  is rapidly ramped back to the initial conducting point, where the oscillator amplitude and phase are measured by mixing with a probe pulse as before.

### Probing electron dynamics in a single quantum dot

Figure 3b shows three ringdown traces, measured with the time-domain scheme described above. All three are pumped and probed at the conducting point as in Fig. 2b, but differ in their gate traverse,  $\Delta V_G$ , during the free propagation stage, taking them to three different points with respect to the Coulomb blockade peak (dashed lines, Fig. 3c,d). The blue trace has zero traverse ( $\Delta V_G = 0$ ) and is

thus identical to the trace in Fig. 2e. The purple trace corresponds to traverse close to the top of the Coulomb blockade peak, showing much faster decay of the ringdown ( $Q = 430$ ). Conversely, when the gate is traversed to the Coulomb valley (orange curve) a much slower decay of the ringdown is observed ( $Q = 4 \times 10^4$ ). The measured ringdown envelope amplitudes,  $A(\tau_{prop})$ , are described well by an exponential decay, whereas measured phase shifts,  $\Delta\phi(\tau_{prop})$ , increase linearly with  $\tau_{prop}$  (Fig. 3b, inset), demonstrating that each ringdown has a well-defined frequency and dissipation that are independent of  $\tau_{prop}$ . From the measured  $\Delta\phi$  and  $A$  after a single  $\tau_{prop}$ , we can thus determine the frequency shift and the dissipation of the mechanical mode during the free propagation period:  $\Delta\omega = \Delta\phi/\tau_{prop}$ ,  $\Gamma = -\log(A/A_0)/\tau_{prop}$ , where  $A_0$  is the measured amplitude for intrinsic mechanical dissipation.

Figure 3c,d shows the frequency and inverse quality factor of the first mechanical mode as a function of  $\Delta V_G$ . The red dots correspond to the CW measurements (fit to Fig. 2a), whereas the blue traces are obtained using the time-domain technique. Clearly, the time-domain technique allows measurement of these quantities for configurations with zero conductance (Coulomb valley) or when the conductance is not gate dependent (Coulomb peak), where the CW mixing techniques are ineffective. Note that during the traverse to the free propagation point, the system often goes through gate voltages for which it has strong interactions with the electronic degrees of freedom. However, the ramp time in our experiment is short enough ( $\sim 20$  ns), as compared to the dissipation rates and frequency shifts at the points with strongest back action ( $\omega/Q \sim (300 \text{ ns})^{-1}$ ), that the expected influence is negligible, as is apparent from the good correspondence between the quantities measured by the CW and time-domain techniques, when both are available.

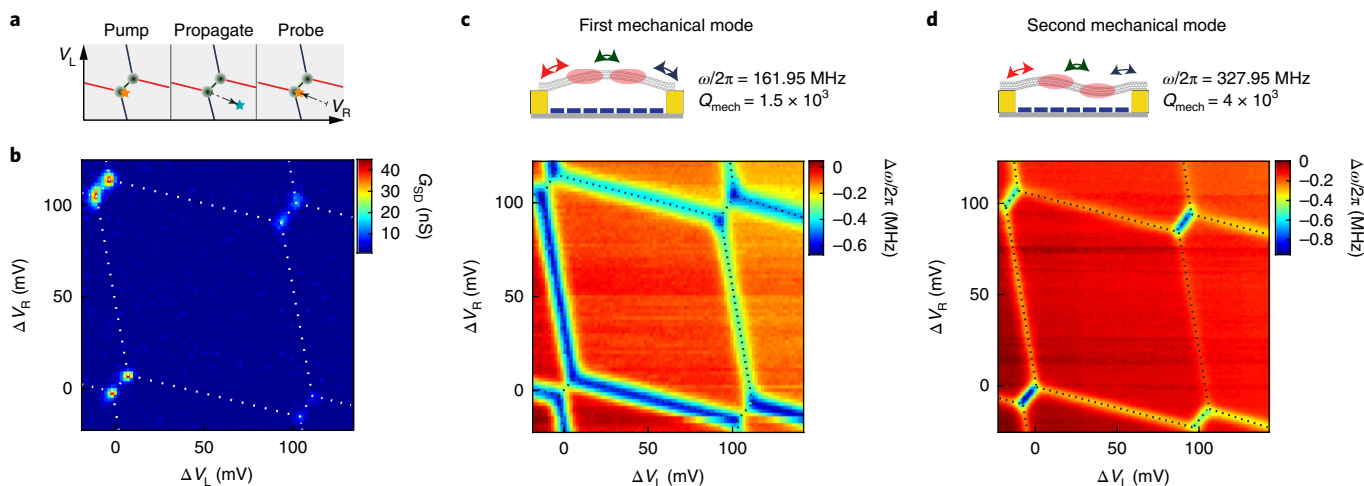


**Fig. 4 | Time-domain measurement of insulating states in a double quantum dot.** **a**, A similar time-domain sequence to that in Fig. 3a is used, only that here both  $V_L$  and  $V_R$  are stepped rapidly between stages, to move from the conducting triple point within the double dot phase diagram in the pumping stage, to any generic point in the two-dimensional voltage space during the free propagation stage, and then back to the triple point for probing and relaxation. **b**, Measured double dot conductance,  $G_{SD}$ , plotted as a function of the gate voltage offsets,  $\Delta V_L$  and  $\Delta V_R$ , from the specific triple point used for pumping in the experiments in the next panels. **c**, Frequency shift,  $\Delta\omega$ , measured using the time-domain scheme as a function of  $\Delta V_L$  and  $\Delta V_R$  when the NT motion is pumped at the first mechanical mode frequency (top illustration). Frequency softening (blue) is seen along the lines that correspond to the different local electronic transitions in the system (red, green and blue arrows in top illustration). **d**, Similar measurement to **c**, but when the NT is driven in the second mechanical mode (top illustration).

### Probing electron dynamics in a double quantum dot

Having established our technique on single quantum dot measurements, we now proceed to probe a double quantum dot. We use a similar pulse sequence as in single dot case, only that here two gate voltages  $V_L$  and  $V_R$  are rapidly ramped to take the double quantum dot from a conducting triple point to an arbitrary point in the two-dimensional voltage space (Fig. 4a). Figure 4b shows the double quantum dot conductance in the region of interest, measured as a function of  $\Delta V_L$  and  $\Delta V_R$ , the voltage offsets from the pumping/probing point. The frequency shifts of the first and second mechanical modes ( $\omega_1 \approx 2\pi \times 161.95$  MHz,  $\omega_2 \approx 2\pi \times 327.95$  MHz) measured with the time-domain technique as a function of  $\Delta V_R$  and  $\Delta V_L$  are shown in Fig. 4c,d. Specifically, we observe negative frequency shifts along three sets of lines (dashed), which correspond to the three electronic transitions in the double quantum dot (illustrated by red, green and blue arrows in the upper diagrams), resulting from the dot occupations responding to the mechanical motion. Whereas transport through the device requires all three transitions to be in resonance, the mechanical motion couples to each of them independently and can thus reveal the transitions even when the system is insulating. A clear difference is observed in the coupling to the two mechanical modes: the first mode is primarily softened along the two transitions which change the total charge in the system (external transitions, red and blue arrows), whereas the second mode is softened primarily along the transition that sloshes an electron between the dots (internal transition, green arrow).

Zooming in on the internal transition, we plot in Fig. 5a the measured frequency shift,  $\Delta\omega$ , and the dissipation rate,  $\Gamma$ , as a function of  $\Delta V_R$  and  $\Delta V_L$ . On the external transition lines, we observe a peak in both  $|\Delta\omega|$  and  $\Gamma$ , similar to the mechanical back action observed in experiments with single dots<sup>24,25</sup>. From the ratio between the softening and the dissipation rates we can determine separately the tunnelling rates between the right (left) dot and its corresponding lead<sup>15</sup>:  $\Gamma_L \sim \Gamma_R \sim 2\pi \times 1.2$  GHz. Notably, the behaviour around the internal transition line is markedly different: whereas the softening,  $|\Delta\omega(\delta V)|$ , has a peak at  $\delta V = 0$  (detuning  $\delta V$  is the distance from the internal transition line), the mechanical dissipation,  $\Gamma(\delta V)$ ,

shows a local minimum at  $\delta V = 0$ , with two symmetric peaks around it. This observed detuning dependence of the frequency shifts and dissipation is at odds with theoretical models that consider the back action due to incoherent tunnelling in single<sup>33,34</sup> and double<sup>15</sup> quantum dots. Simulating our system using such a model (Fig. 5b) yields a singly peaked  $\Delta\omega(\delta V)$  and  $\Gamma(\delta V)$ .

### Theoretical model

To explain the observation, coherent tunnelling between the dots needs to be included. The observed result was predicted<sup>28</sup> in a simple model treating the two states connected by internal transition as a two-level system defined by detuning  $\delta V$  and the coherent tunnelling amplitude  $t_c$ . Although the physical system has additional spin and valley degrees of freedom, strong electron–electron interactions in suspended carbon NTs push the electrons away from each other into a Wigner molecule state<sup>3</sup>, reducing the exchange interaction, and making the charge sector behave independently of the spin and valley degrees of freedom. Consequently, the simplified two-level model suffices to describe the observed behaviour (Supplementary Section 3).

At large detuning ( $\delta V \gg t_c$ ), the back action on mechanics is similar to that observed in previous incoherent experiments, due to changes in charge occupation that lag after the mechanical motion. However, for small detuning, the coherent tunnelling will dominate, giving a finite frequency shift without dissipation. In this limit, the electronic back action results from adiabatic modulation of the electronic wavefunction, rather than from the changes in the occupations of the dots. The former is not retarded with respect to the mechanical motion, and thus does not produce dissipation (Supplementary Section 8). When coherent tunnelling is added to our simulations (Fig. 5c) we indeed observe that they reproduce the measurement over the full voltage range (fit details in Supplementary Section 6).

Figure 5d shows traces of  $\Delta\omega$  and  $\Gamma$  measured as a function  $\delta V$  along the dashed line in Fig. 5a, for varying voltages on the central gate that change  $t_c$ . With increasing  $t_c$  we can see that the width of the dip in dissipation increases. From a fit to the theory (solid lines)

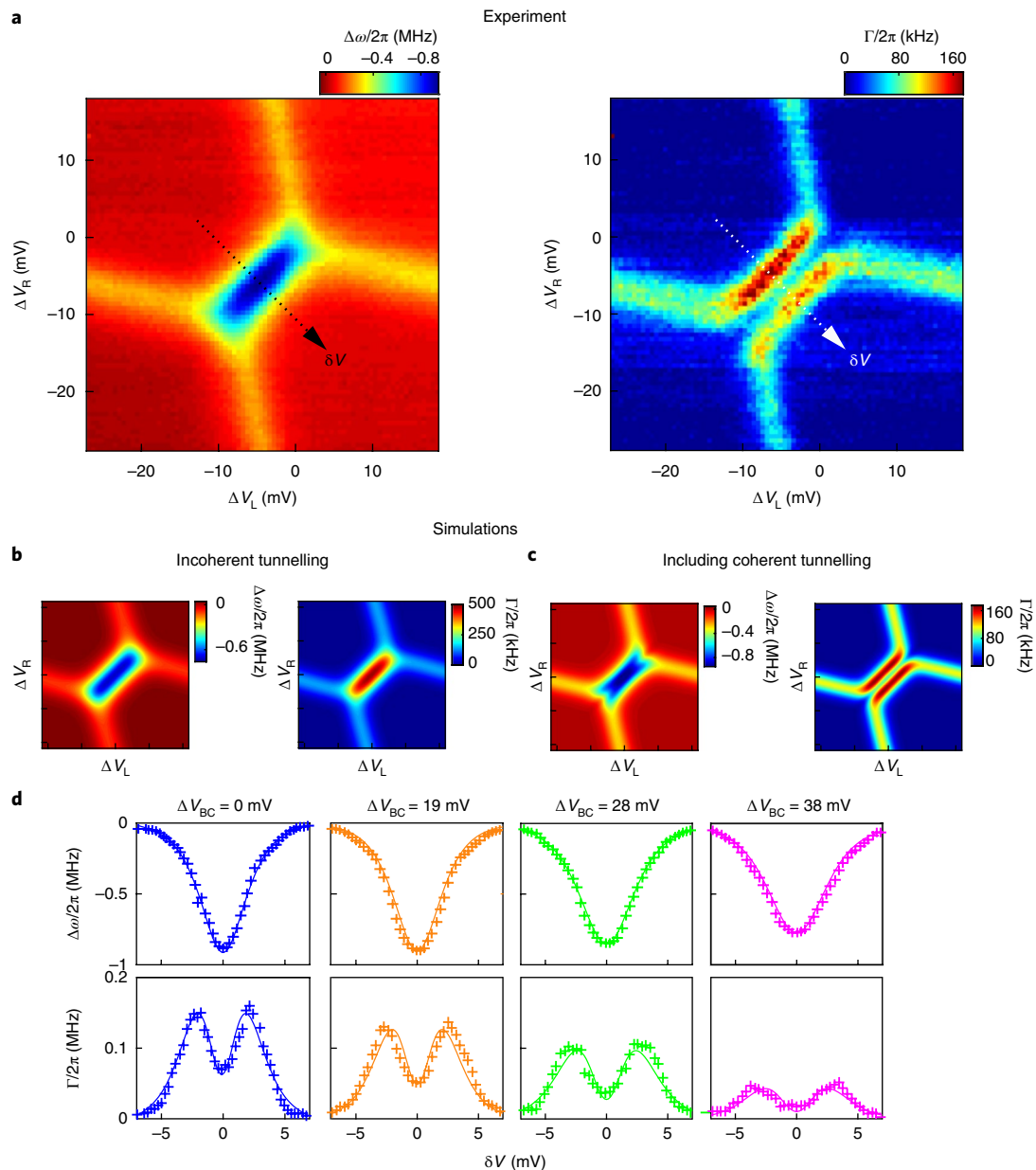


**Fig. 5 | Coupling between nanomechanics and a coherently-tunnelling electron in a double quantum dot. a**, Measured frequency shift,  $\Delta\omega$  (left), and dissipation rate,  $\Gamma$  (right), as a function of  $\Delta V_R$  and  $\Delta V_L$  for the second mechanical mode around the charge degeneracy line between the charge states  $(n_L, n_R), (n_L - 1, n_R + 1)$  of the double dot. **b**, Simulated  $\Delta\omega$  and  $\Gamma$  around the vertex, including incoherent tunnelling of an electron between the dots (Supplementary Section 7). **c**, Same with coherent tunnelling. **d**, Measured  $\Delta\omega$  and  $\Gamma$  as a function of detuning gate voltage,  $\delta V$ , along the dashed line in **a** (crosses). The four subpanels correspond to different voltage steps applied on the centre gate during the free propagation time,  $\Delta V_{BC} = 0, 19, 28, 38$  mV, changing the central barrier height during the experiment. Solid lines are fits to a full theory that includes coherent and incoherent tunnelling (see main text and Supplementary Section 6, 8).

we can extract the incoherent tunnelling rate,  $T_1^{-1}/2\pi \approx 0.5$  GHz, the bare coupling  $g_0/2\pi \approx 320$  MHz, and the values of coherent tunnelling ranging from  $t_c/2\pi = 49$  GHz to  $t_c/2\pi = 96$  GHz for the four traces. These numbers verify that coherent tunnelling dominates over the incoherent one in our measurements.

### Discussion and conclusions

The technique demonstrated above can be used for studying various insulating states that are challenging to probe via transport. A particularly interesting example, which is well-suited for studying by our technique, is the electronic Wigner crystal in carbon NTs.

The smoking gun signature of this crystal is its periodic charge ordering in real space. Our method should allow probing the response of this crystal to periodic perturbation commensurate with its period, formed by a corresponding mechanical mode, a direct generalization of the probing of the single electron response to the second mechanical mode, performed here. This method holds key advantages for probing such a fragile insulating state: it minimally perturbs the measured state as compared to scanning probes, can reach high spatial resolution, limited only by the frequency of the accessible phononic modes, and may resolve the dynamics on relatively short timescales. The charge sensitivity demonstrated in the

experiments above is  $10^{-4} q_e / \sqrt{\text{Hz}}$  ( $q_e$  is the electron charge) projected on the mechanical motion mode (Supplementary Section 5), which compares favourably with local charge probes, and with the expected charge displacement in this system. This sensitivity can improve substantially by decreasing the temperature ( $\times 100$  improvement in Q-factor) and applying stronger electric fields ( $\times 100$ ), which will make it even more advantageous for measuring fine features of insulating states. Other potential applications of the technique in carbon NTs include expected charge reordering signatures of insulating states, such as the dielectric response of a Mott insulator<sup>17</sup>, the appearance of a ferroelectric dipole moment, which is the hallmark of the excitonic insulator<sup>5</sup>, and possible charge signatures at the topological transitions in one dimension<sup>35,36</sup>. More broadly, the method can be used in other suspended one- and two-dimensional systems<sup>6,37</sup>, to probe similar charge reordering phenomena in overall insulating states, such as Wigner crystallization in suspended graphene<sup>38</sup>, opening a new experimental window for exploring a growing number of unconventional insulating states that are being discovered in low-dimensional materials.

### Online content

Any methods, additional references, Nature Research reporting summaries, source data, statements of data availability and associated accession codes are available at <https://doi.org/10.1038/s41565-018-0341-6>.

Received: 13 October 2017; Accepted: 23 November 2018;

Published online: 14 January 2019

### References

- Deshpande, V. V. et al. Mott insulating state in ultraclean carbon nanotubes. *Science* **323**, 106–110 (2009).
- Deshpande, V. V. & Bockrath, M. The one-dimensional Wigner crystal in carbon nanotubes. *Nat. Phys.* **4**, 314–318 (2008).
- Pecker, S. et al. Observation and spectroscopy of a two-electron Wigner molecule in an ultraclean carbon nanotube. *Nat. Phys.* **9**, 576–581 (2013).
- Shafir, I. et al. Imaging the Wigner crystal of electrons in one dimension. Preprint at <https://arxiv.org/abs/1803.08523> (2018).
- Varsano, D. et al. Carbon nanotubes as excitonic insulators. *Nat. Commun.* **8**, 1461 (2017).
- Chen, C. et al. Modulation of mechanical resonance by chemical potential oscillation in graphene. *Nat. Phys.* **12**, 240–244 (2016).
- Cao, Y. et al. Unconventional superconductivity in magic-angle graphene superlattices. *Nature* **556**, 43–50 (2018).
- Ash, E. A. & Nicholls, G. Super-resolution aperture scanning microscope. *Nature* **237**, 510–512 (1972).
- Yoo, M. J. Scanning single-electron transistor microscopy: imaging individual charges. *Science* **276**, 579–582 (1997).
- LaHaye, M. D., Suh, J., Echternach, P. M., Schwab, K. C. & Roukes, M. L. Nanomechanical measurements of a superconducting qubit. *Nature* **459**, 960–964 (2009).
- Rugar, D., Budakian, R., Mamin, H. J. & Chui, B. W. Single spin detection by magnetic resonance force microscopy. *Nature* **430**, 329–332 (2004).
- Huttel, A. K. et al. Carbon nanotubes as ultrahigh quality factor mechanical resonators. *Nano. Lett.* **9**, 2547–2552 (2009).
- Moser, J., Eichler, A., Güttinger, J., Dykman, M. I. & Bachtold, A. Nanotube mechanical resonators with quality factors of up to 5 million. *Nat. Nanotech.* **9**, 1007–1011 (2014).
- Moser, J. et al. Ultrasensitive force detection with a nanotube mechanical resonator. *Nat. Nanotech.* **8**, 493–496 (2013).
- Benyamini, A., Hamo, A., Kusminskiy, S. V., von Oppen, F. & Ilani, S. Real-space tailoring of the electron-phonon coupling in ultraclean nanotube mechanical resonators. *Nat. Phys.* **10**, 151–156 (2014).
- Schneider, B. H., Singh, V., Venstra, W. J., Meerwaldt, H. B. & Steele, G. A. Observation of decoherence in a carbon nanotube mechanical resonator. *Nat. Commun.* **5**, 5819 (2014).
- Okazaki, Y., Mahboob, I., Onomitsu, K., Sasaki, S. & Yamaguchi, H. Gate-controlled electromechanical backaction induced by a quantum dot. *Nat. Commun.* **7**, 11132 (2016).
- Deng, G. W. et al. Strongly coupled nanotube electromechanical resonators. *Nano. Lett.* **16**, 5456–5462 (2016).
- Ares, N. et al. Resonant optomechanics with a vibrating carbon nanotube and a radio-frequency cavity. *Phys. Rev. Lett.* **117**, 170801 (2016).
- Knobel, R. G. & Cleland, A. N. Nanometre-scale displacement sensing using a single electron transistor. *Nature* **424**, 291–293 (2003).
- Zhu, J., Brink, M. & McEuen, P. L. Frequency shift imaging of quantum dots with single-electron resolution. *Appl. Phys. Lett.* **87**, 242102 (2005).
- Stomp, R. et al. Detection of single-electron charging in an individual InAs quantum dot by noncontact atomic-force microscopy. *Phys. Rev. Lett.* **94**, 056802 (2005).
- Naik, A. et al. Cooling a nanomechanical resonator with quantum backaction. *Nature* **443**, 193–196 (2006).
- Lassagne, B. et al. Coupling mechanics to charge transport in carbon nanotube mechanical resonators. *Science* **325**, 1107–1110 (2009).
- Steele, G. A. et al. Strong coupling between single-electron tunneling and nanomechanical motion. *Science* **325**, 1103–1107 (2009).
- Bennett, S. D., Cockins, L., Miyahara, Y., Grütter, P. & Clerk, A. A. Strong electromechanical coupling of an atomic force microscope cantilever to a quantum dot. *Phys. Rev. Lett.* **104**, 017203 (2010).
- Castellanos-Gomez, A., Meerwaldt, H. B., Venstra, W. J., van der Zant, H. S. J. & Steele, G. A. Strong and tunable mode coupling in carbon nanotube resonators. *Phys. Rev. B* **86**, 041402 (2012).
- Gardner, J., Bennett, S. D. & Clerk, A. A. Mechanically probing coherent tunneling in a double quantum dot. *Phys. Rev. B* **84**, 205316 (2011).
- Waissman, J. et al. Realization of pristine and locally tunable one-dimensional electron systems in carbon nanotubes. *Nat. Nanotech.* **8**, 569–574 (2013).
- de-Picciotto, R. et al. Direct observation of a fractional charge. *Nature* **389**, 162–164 (1997).
- Wiel, Wvander & Franceschi, S. De Electron transport through double quantum dots. *Rev. Mod. Phys.* **75**, 1–22 (2002).
- Sazonova, V. et al. A tunable carbon nanotube electromechanical oscillator. *Nature* **431**, 284–287 (2004).
- Armour, a, Blencowe, M. & Zhang, Y. Classical dynamics of a nanomechanical resonator coupled to a single-electron transistor. *Phys. Rev. B* **69**, 125313 (2004).
- Clerk, A. A. & Bennett, S. Quantum nanoelectromechanics with electrons, quasi-particles and Cooper pairs: effective bath descriptions and strong feedback effects. *New J. Phys.* **7**, 238 (2005).
- Efroni, Y., Ilani, S. & Berg, E. Topological transitions and fractional charges induced by strain and a magnetic field in carbon nanotubes. *Phys. Rev. Lett.* **119**, 147704 (2017).
- Lotfzadeh, N., Senger, M. J., McCulley, D. R., Minot, E. D. & Deshpande, V. V. Sagnac electron interference as a probe of electronic structure. Preprint at <https://arxiv.org/abs/1808.01341> (2018).
- He, R., Feng, X. L., Roukes, M. L. & Yang, P. Self-transducing silicon nanowire electromechanical systems at room temperature. *Nano. Lett.* **8**, 1756–1761 (2008).
- Padhi, B., Setty, C. & Phillips, P. W. Doped twisted bilayer graphene near magic angles: proximity to Wigner crystallization not Mott insulation. Preprint at <https://arxiv.org/abs/1804.01101> (2018).

### Acknowledgements

We thank A. Bachtold, F. Pistolesi and F. von Oppen for stimulating discussions and D. Mahalu for the e-beam writing. We further acknowledge support from the Minerva Foundation grant (712290).

### Author contributions

I.K. performed the experiments and analysed the data. I.K. and S.I. designed the experiments. I.K. and A.A.C. wrote the theoretical model. I.K. performed the numerical simulations. I.K., A.A.C. and S.I. contributed to its theoretical interpretation. I.K. and S.I. wrote the paper.

### Competing interests

The authors declare no competing financial interests.

### Additional information

Supplementary information is available for this paper at <https://doi.org/10.1038/s41565-018-0341-6>.

Reprints and permissions information is available at [www.nature.com/reprints](http://www.nature.com/reprints).

Correspondence and requests for materials should be addressed to S.I.

**Publisher's note:** Springer Nature remains neutral with regard to jurisdictional claims in published maps and institutional affiliations.

© The Author(s), under exclusive licence to Springer Nature Limited 2019

## Methods

**Device fabrication.** Devices were fabricated using our nano-assembling technique, presented in detail in ref. <sup>29</sup>. Specifically, the nanotubes were grown from catalyst using chemical vapour deposition following a standard recipe for single-walled nanotubes, with argon hydrogen and ethylene gases. The circuits were patterned on a Si/SiO<sub>2</sub> wafer using electron-beam lithography, followed by the evaporation of contacts (5 nm/85 nm Cr/PdAu), gates (4 nm/25 nm Cr/PdAu) and deep reactive

ion etching. The device consisted of a NT assembled over a pair of 1.5- $\mu$ m-wide contacts and suspended 1.2  $\mu$ m between them at a height of 60 nm above seven gates with 150 nm periodicity.

## Data availability

The data that support the plots within this paper and other findings of this study are available from the corresponding author upon request.